ROYAL SOCIETY OF CHEMISTRY

## PAPER

Check for updates

# *In situ* observation of the magnetocaloric effect through neutron diffraction in the Tb(DCO₂)₃ and TbODCO₃ frameworks†

Richard J. C. Dixey,[ab] Pascal Manuel,[c] Fabio Orlandi,[c] Paromita Mukherjee,[d] Siân E. Dutton,[d] Gavin B. G. Stenning[c] and Paul J. Saines ⋆[a]

Probing the magnetic structure of magnetocaloric materials in applied fields, can reveal detailed insight into the mechanism of magnetic refrigeration thereby linking the magnetic states that form under applied magnetic fields to changes in magnetic entropy. This study probes the long range magnetic order in Tb(DCO₂)₃ and TbODCO₃ as a function of temperature and applied magnetic field, through neutron diffraction measurements. A triangular Ising antiferromagnetic phase is formed, in small applied magnetic fields in Tb(DCO₂)₃, a spin flip transition occurs to a simple ferromagnetic structure in higher applied fields. TbODCO₃ undergoes a phase transition, in applied fields, into two magnetic phases; namely a buckled chain ferromagnetic phase along the *b*-axis and a canted antiferromagnetic phase, with a ferromagnetic component along *c*-axis. Both of the states observed in TbODCO₃ are consistent with Ising-like anisotropy previously reported in TbODCO₃ and the coexistance of these is likely the result of applying a magnetic field to a powdered sample.

## Introduction

Advanced functional magnetic materials with finely tuned properties are relevant to a broad range of modern technologies, finding applications from data storage/transfer[1–3] to medicine.[4] Optimising such materials, including multiferroics[5–7] and magnetocalorics,[8–11] requires a detailed understanding of how they respond to an applied magnetic field. There is also great fundamental interest in magnetic phenomena that emerge with increasing applied magnetic fields, including metamagnetic spin–flop and spin–flip transitions,[12–16] exotic magnetic states in Ising 1D chains and magnetisation plateaus.[17–21] Since the bulk magnetic properties of a material are ultimately driven by the atomic level structure,[8,22] understanding how the magnetic correlations in materials changes under applied magnetic fields is essential for innovation.

The magnetocaloric effect (MCE) is an entropically driven temperature change observed in all magnetic materials when a magnetic field is applied and removed.[11,23] In paramagnetic magnetocalorics the application of a magnetic field drives a phase transition to a highly ordered phase, which is often thought to resemble a field induced ferromagnet. This reduces the number of microstates ($\Omega$) and the magnetic entropy ($S$), causing a change in temperature proportional to $R \ln \Omega$. This effect can be used in devices, as an energy efficient alternative to vapour compression refrigeration.[24] The MCE has been extensively studied in a multitude of compounds since its discovery in 1917,[25] but this is mostly limited to bulk property studies.[11] Magnetic field induced phase transitions are well established in magnetocaloric materials such as Ho₃Ga₅O₁₂ and Ho₃CrGa₄O₁₂,[26–28] where strong Ising anisotropy has been shown to be an important factor in the magnetocaloric behaviour with respect to field while quasi-1D materials, such as CoV₂O₆, have also shown excellent magnetocaloric properties.[21] It is well established that frustrated magnetism, where conflicting magnetic interaction prevent a single ordered ground state from emerging, can improve the MCE by allowing a denser packing of magnetic cations, as shown in the benchmark material Gd₃Ga₅O₁₂.[29,30] It is not easy to understand, however, how the large number of degenerate ground states of a particular material will be affected by the applied magnetic field and therefore the nature of the long range ordered states formed under this stimuli.[31] Therefore, understanding microscopic

*ᵃ School of Physical Sciences, Ingram Building, University of Kent, Canterbury, CT2 7NH, UK. E-mail: P.Saines@kent.ac.uk*

*ᵇ Centre for Condensed Matter and Material Physics, School of Physics and Astronomy, Queen Mary University of London, Mile End Rd, London, E1 4NS, UK*

*ᶜ ISIS Facility, STFC Rutherford Appleton Laboratory, Chilton, Didcot, OX11 0QX, UK*

*ᵈ Cavendish Laboratory, University of Cambridge, JJ Thomson Avenue, Cambridge, CB3 0HE, UK*

† Electronic supplementary information (ESI) available: Tables and figures of crystallographic details and local magnetic structure refinements. See DOI: 10.1039/d0tc03153d

This journal is © The Royal Society of Chemistry 2020

*J. Mater. Chem. C*, 2020, **8**, 12123–12132 | **12123**

changes in the magnetic states of high performance magneto-calorics is key.

The $Ln(HCO_2)_3$ and $LnOHCO_3$ frameworks (where Ln = Gd, Tb, Dy, Ho, Er) are both highly efficient and promising magneto-caloric materials over a wide temperature range (2–20 K) making them suitable alternatives to liquid helium cooling, for scientific and medical applications.[8,32–34] Both $Tb(HCO_2)_3$ and $AOHCO_3$ (A = Tb or Dy) outperform their high performance Gd analogues above 4 K, in applied fields that can be generated by a permanent magnet (below 2 T). The performance of the $AOHCO_3$ phases are particularly impressive, retaining a greater magnetocaloric effect than the benchmark $Gd_3Ga_5O_{12}$ up to nearly 10 K.[33] In order to fully appreciate the subtleties of the magnetocaloric effect mechanism in these materials, it is important to understand the magnetic phases that develop in the presence of an applied magnetic field. Fig. 1 highlights the triangular motifs present in the $LnOHCO_3$ and $Ln(HCO_2)_3$ frameworks that have been suggested to cause the frustrated magnetic interactions in these materials, that play a key role in their MCE effectiveness.[8,33]

We have previously established the magnetic states that form in both $Tb(HCO_2)_3$ and $TbOHCO_3$ in the absence of applied magnetic fields.[9,35] $Tb(HCO_2)_3$, which adopts $R3m$ rhombohedral symmetry at all measured temperatures,[36] shows strong diffuse scattering indicative of short range order below 20 K, where its magnetocaloric effect begins to be significant. This short range order is formed of ferromagnetically coupled linear chains of Ising-like moments aligned along the $c$-axis, antiferromagnetically coupled in a triangular array within the $ab$ plane.[8,33] Below 1.6 K it displays long range 1D order along the $c$-axis and the chain direction, and finite correlations in the $ab$ plane, extending $\sim 50$ Å.[8,36] Long range order appears to be prevented by the frustrated interactions between chains leading to the emergence of a triangular Ising antiferromagnetic (TIA) state. $TbODCO_3$, which adopts $P2_12_12_1$ orthorhombic symmetry, also shows strong diffuse scattering below 20 K attributed to the formation of ferro-magnetic correlations between the Ising-like cations in the buckled ferromagnetic chains along the $b$-axis, which are packed into an antiferromagnetic triangular like lattice.[9] These buckled chains

present an additional source of entropy in these systems, potentially responsible for the higher magnetocaloric effect observed.[33] Below 1.2 K physical property measurements indicate the emergence of an ordered state and, in the isostructural $HoODCO_3$, corresponds to a quasi-long range ordered antiferromagnet.[9]

It has been proposed that the suppression of the frustrated antiferromagnetic interactions in $Tb(HCO_2)_3$ and $TbOHCO_3$ enable high entropy changes in small applied magnetic fields.[8,33] This is consistent with the rapid increases in their magnetisation under modest fields,[8,33] contributing to a high efficiency as a magnetocaloric.[36] The mechanism for the magnetocaloric cycle in these materials, has not been experimentally observed. Neutron diffraction is the obvious method for probing the magnetic structure of these materials due to its sensitivity to magnetic moments. Therefore, in this study we have investigated the magnetic structure of these materials under applied fields. We have identified the ordered phases in these materials as a function of temperature and applied field, in order to understand how the microscopic interactions affect the magnetic entropy of the system. The diffraction patterns of $Tb(DCO_2)_3$ indicate it undergoes a phase transition from a correlated para-magnetic state through the disordered TIA phase to a fully ferromagnetic phase. Application of magnetic fields to $TbODCO_3$, in contrast, leads to the coexistence of a ferromagnetic phase, with spins along the $b$-axes, and a canted antiferromagnetic phase, with a weak ferromagnetic component and the same easy axis. This establishes the magnetic states responsible for the efficient magnetocaloric effect of these materials in low applied fields, providing key insights into how these materials could be further enhanced.

## Experimental methods

It is necessary to deuterate neutron samples to minimise the background caused by the incoherent scattering of hydrogen. We expect the deuteration of the framework for neutron studies will have an insignificant effect on the magnetic exchange correlations. $Tb(DCO_2)_3$ was synthesized by slowly adding 2 g of $Tb(NO_3)_3 \cdot 6H_2O$ (99.9%, Sigma-Aldrich) to a solution of 4.75 mL of D-formic acid (95.0% Sigma-Aldrich), with 0.25 mL of ethanol added. After several minutes of stirring, $NO_x$ was released and the product precipitated out of solution. The products were collected by vacuum filtration, washed several times with ethanol, and dried in a desiccator.

$TbODCO_3$ was synthesised via a hydrothermal method, by reacting $Tb(NO_3)_3 \cdot 6H_2O$ (99.9%, Sigma-Aldrich, 1 mmol) and $Na_2CO_3$ (99.5%, Sigma-Aldrich, 1 mmol) in $D_2O$ (99.9%, Sigma-Aldrich, 10 mL). The mixture was sealed in a Teflon-lined (23 mL) Parr-Bomb autoclave and heated at 170 °C for 72 h, followed by cooling to room temperature at a rate of 3 °C h$^{-1}$. The samples were isolated by vacuum filtration, washed with $D_2O$ and dried in a desiccator. 2 g deuterated samples were produced under an $N_2$ atmosphere in multiple batches.

The magnetic measurements of the hydrogenated poly-crystalline samples ($\sim 20$ mg) were performed using Quantum Design MPMS SQUID magnetometers. Samples were placed in
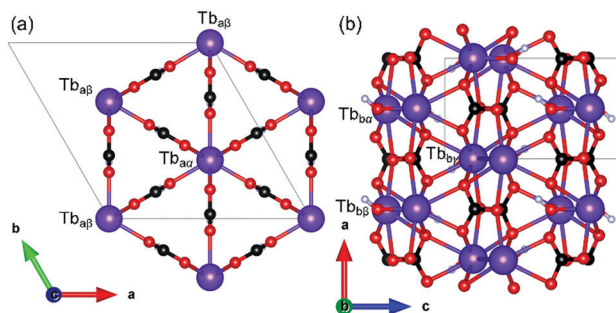


**Fig. 1** Diagrams of the nuclear structure of (a) $Tb(DCO_2)_3$ and (b) $TbODCO_3$ viewed down the triangular packing of chains. The Tb, C, O and D atoms are shown in purple, black, red and grey, respectively. Tb–Tb distances in $Tb(DCO_2)_3$ are 6.16 Å, and 6.57 Å between $Tb_{a\alpha}$–$Tb_{a\beta}$ and $Tb_{a\beta}$–$Tb_{a\beta}$ respectively. Tb–Tb distances in $TbODCO_3$ are 4.84, 5.09 and 5.13 Å, between $Tb_{b\alpha}$–$Tb_{b\beta}$, $Tb_{b\beta}$–$Tb_{b\gamma}$, and $Tb_{b\alpha}$–$Tb_{b\gamma}$, respectively connected though a $CO_3$. However, distances between hypothetical chains are equal in both materials.

**12124** | *J. Mater. Chem. C*, 2020, **8**, 12123–12132

This journal is © The Royal Society of Chemistry 2020

gelatin capsules enclosed inside a pierced straw with a uniform diamagnetic background. Variable field measurements above 2 K were measured on a standard MPMS, and measurements below 2 K were performed using a MPMS magnetometer, with a $^3$He insert. Low field and high field data on TbOHCO$_3$ at 0.5 K, were collected in two measurements.

Powder neutron diffraction measurements were carried out on the high-resolution time-of-flight (TOF) WISH diffractometer at the ISIS neutron source, Rutherford Appleton Laboratory.[37] Measurements were carried out between 1.5 K to 40 K, and applied magnetic fields between 0–3 T, generated using the Oxford instrument 10 T cryomagnet. Powders were loaded into 8 mm vanadium cans, wetted with d$_6$-isopropyl alcohol, sealed with indium wire and flash frozen using the cryomagnet. The d$_6$-isopropyl alcohol successfully minimised the effect of preferred orientation on the diffraction patterns in the application of the magnetic field. The sample was flash frozen in order to prevent the d$_6$-isopropyl alcohol crystallisation and resulted in the formation of an amorphous solid, as indicated by the diffuse scattering centred around 4.2 Å.

Neutron absorption of Tb(DCO$_2$)$_3$ and TbODCO$_3$ were negligible and so corrections were only applied during Rietveld refinements. Rietveld refinements were performed in FULLPROF.[38,39] Aluminium reflections of the cryomagnet, were fitted with a Le Bail model to negate the effects of the highly textured surface,[40] and un-indexable peaks in the highest resolution bank were excluded from refinements. A linear interpolation of points were used to fit the background and a convolution of back-to-back exponentials with a pseudo-Voight TOF function was used to fit the diffraction peak shapes. The full width half-maximums of the magnetic peaks were fit with an anisotropic broadening model.[41] Symmetry analysis and determination of allowed magnetic structures was performed using the Bilbao Crystallographic server.[42] Due to a 1:1 correlation between phase fraction and moment size, diffraction patterns with coexisting magnetic phases were fitted by fixing the phase fraction of each magnetic phases to be equal, and the vectors refined. The moment lengths refined are directly tied to this constraint.

## Results and discussion

### Magnetic property measurements

It has previously been shown that Tb(HCO$_2$)$_3$ and TbOHCO$_3$ undergo transitions to the TIA phase at ∼1.6 K and an antiferromagnetic state at ∼1.2 K, respectively.[9,36,43] Above their ordering temperatures these materials both contain short range ferromagnetic Ising chains in the correlated paramagnetic phase, asserted to be responsible for their highly efficient magnetocaloric effects.[8,9] Variable field measurements above and below these transitions show features suggestive of the ordering behaviour. For magnetic measurements on a powder averaged lanthanide material with uniaxial Ising-like spin anisotropy, such as Tb(HCO$_2$)$_3$,[36] we should expect the bulk magnetisation to approach 4.5 $\mu_B$, as shown in eqn (1).

$$\frac{1}{N}\sum_{i=0}^{i=2\pi} g_J J \sin^2\theta_i = 0.5 g_J J \tag{1}$$

The equation for the expected magnetisation saturation value for a magnetic material with a single uniaxial spin orientation and Ising-like spin anisotropy, where is the angle of the $i$th spin vector. For Tb$^{3+}$, where $J = 6$ and $g_j = 3/2$, $0.5 g_J J = 4.5$ $\mu_B$.

This however, does not apply to TbOHCO$_3$ which has been shown to have 4 Ising axes.[9] This is broadly in agreement to the saturation values of Tb(HCO$_2$)$_3$ in applied fields above 1 T, as shown in Fig. 2, but some field induced breaking of the anisotropy is likely introduced in higher fields. Little difference can be seen in magnetisation behaviour of Tb(HCO$_2$)$_3$ between the 2 K data and the lower temperature data in the ordered phases. This can be attributed to the reported quasi-1D Ising like nature of the spins in Tb(HCO$_2$)$_3$,[36,43] requiring small fields before the frustrated antiferromagnetic correlations are overcome prior to forming a ferromagnetic phase. Therefore, even in the ordered phase the frustrated ground state is prone to the formation of a ferromagnetic phase upon perturbation through an applied field. This is consistent with the reported behaviour of Tb(HCO$_2$)$_3$, and provides a strong evidence to hypothesis that frustrated Ising chains are a recipe for enhanced magnetocaloric materials. In contrast, TbOHCO$_3$ shows considerable differences in magnetisation behaviour between 0.5 K and 2.0 K, where in the absence of an applied magnetic field ordered antiferromagnetic and correlated paramagnetic phases exist, despite both containing ferromagnetic Ising chains. TbOHCO$_3$ shows a steeper magnetisation, and a higher saturation value in the paramagnetic phase, likely due to the strong ferromagnetic correlations along the chain directions but much weaker frustrated antiferromagnetic correlations.[9] At lower temperatures where the antiferromagnetic correlations become more significant, a lower saturation value is observed.

TbOHCO$_3$ has been reported to contain four Ising axes, and therefore the saturation value of the bulk powder sample is expected to be larger than that of Tb(HCO$_2$)$_3$. We observe a
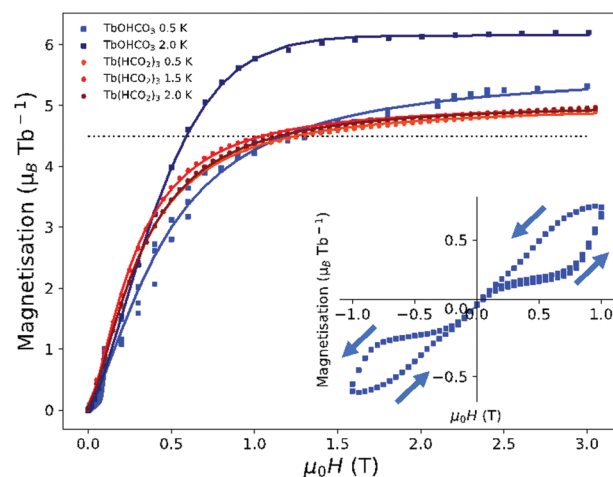


**Fig. 2** Applied field measurements of Tb(HCO$_2$)$_3$ and TbOHCO$_3$ at various temperatures, above and below the magnetic phase transitions. Points in red shades indicate Tb(HCO$_2$)$_3$, and squares in blue shades indicate TbOHCO$_3$. Hysteresis of TbOHCO$_3$, in small applied fields at 0.5 K shown in the insert. Dotted line indicates $0.5 g_J J$ for Tb$^{3+}$. Arrows indicate direction of magnetisation.

This journal is © The Royal Society of Chemistry 2020

*J. Mater. Chem. C,* 2020, **8**, 12123–12132 | **12125**

saturation value slightly larger than that of $Tb(HCO_2)_3$ and approaching $2/3g_JJ$. As shown in the insert of Fig. 2, $TbOHCO_3$ also shows an additional magnetisation plateau at $\sim 0.2\ \mu_B$ equal to $M/M_{sat} = 1/30$. This plateau is not seen in the 2 K data, and emerges as a result of the effect of a field on the magnetic ground state. The exact nature of the plateau is currently unknown and should be subject to further investigations. Similar magnetisation plateaus have been observed in other rare earth,[44,45] and magnetocaloric materials.[46,47] In these low applied fields, some magnetic hysteresis is observed indicating a ferromagnetic component to the field induced magnetic phase. A 1/3 magnetisation plateau is sometimes observed in Ising chains materials, such as $Ca_3Co_2O_6$, and single crystals or aligned powders of $CoV_2O_6$ (but not polycrystalline samples).[21,48–51] This plateau is a result of a field induced metamagnetic ferrimagnetic state when Ising chains are arranged in a triangle. This plateau can be lost or greatly diminished in polycrystalline samples,[21,50,51] therefore we postulate this is not observed here due to the loss of information associated with powder averaging. However, we may expect to recover these plateaus with magnetic fields applied to the $c$ and $b$ axes of $Tb(HCO_2)_3$ and $TbOHCO_3$ single crystals, respectively along the chain direction.

To investigate the mechanism of the magnetisation behaviours in these magnetocaloric materials, and how this affects the adiabatic refrigeration cycle, we investigated these materials through neutron diffraction in applied fields. This was performed at the temperatures at which they are correlated paramagnets and where the MCE is most significant.

### $Tb(DCO_2)_3$

**Field sweep.** $Tb(DCO_2)_3$ was cooled from room temperature to 1.5 K, and no significant change in the Bragg-like reflections was observed (see Fig. S1 and S2 for fits to these patterns, ESI†). This suggests the TIA has not formed, in a notionally zero applied field, despite having been previously observed to form below 1.6 K.[8,43] This could be a result of a discrepancy in the measured temperatures of different cryostats, poorer temperature equilibration due to the $d_6$-IPA glass not properly conducting heat or a result of trapped magnetic flux present within the magnet affecting the formation of the TIA state at very low applied fields. While it remains present it was also not possible to accurately measure the diffuse scattering previously found in $Tb(DCO_2)_3$,[43] at low temperatures in this study, due to the higher background of these measurements from the sample environment and scattering from the amorphous frozen $d_6$-IPA, which is strongest at $d$-spacings close to where the magnetic diffuse occurs.

At 1.5 K the magnetic field was swept from 0–3 T in variable steps. With an applied field of $\mu_0H = 0.1$ T, the appearance of new peaks was noted (see Fig. 3) and was found to be consistent with the formation of a magnetic phase that can be indexed with the $\mathbf{k}_1$-vector = (0,0,1). These peaks are consistent with the presence of the previously reported TIA phase, suggesting the same phase is being formed.[8,36,43]

Refinement of the TIA phase, requires both the sharp, Bragg-like, and broad diffuse magnetic scattering to be simultaneously fitted, which is not possible with the data obtained in this study
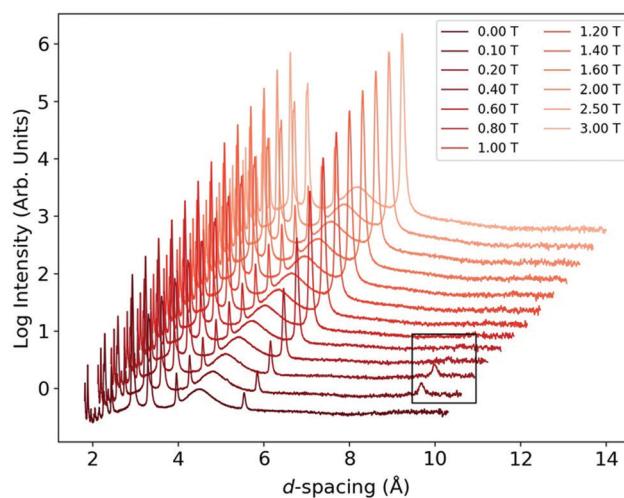


**Fig. 3** Waterfall plot of data from bank 2/9 of WISH, plotted on a log scale and offset for clarity, for $Tb(DCO_2)_3$ with respect to field, at 1.5 K. The peaks at $\sim 5.2$ Å indicate the ferromagnetic phase, and the peaks highlighted with a box at $\sim 9.1$ Å indicate the TIA phase.

since, as explained above, it was not possible to precisely measure the diffuse scattering. As discussed in the study by Saines *et al.*,[8] which was carried out without an applied field, when treated using conventional crystallographic approaches two possible magnetic phases can be fitted to the Bragg-like features. Both of these adopt $P3m'1$ magnetic symmetries, featuring ferromagnetic chains with spins aligned along the $c$-axis and antiferromagnetic alignment of these chains. The two magnetic phases vary only by the choice of the internal phase, to which diffraction is insensitive, with $\pi/6$ consisting of the $\frac{1}{2}$ up, $\frac{1}{2}$ up, down spin or $\pi/4$ consisting of up, down, zero spin structure on a triangle, with the latter resembling a partially disordered antiferromagnet (PDA). The growth of this magnetic phase with applied magnetic field and its appearance together with a $\mathbf{k} = 0$ propagation vector, indicate that the magnetic phase must couple with the field. Considering only these two conventional magnetic structures, this suggests that the magnetic phase present here is the $\frac{1}{2}$ up, $\frac{1}{2}$ up, down phase. As expected, we find either of these models give a good fit to the data obtained here (see Fig. S3–S8, ESI†), but unambiguous determination of this is impossible from diffraction data alone.[36] In any case we note that both these conventional crystallographic models are likely simplifications of the TIA state, which is considered to be a better model of this phase as it also fits the observed diffuse magnetic scattering that was clearly characterised in zero field data,[43] but is also evident here (see Fig. S9, ESI†). We will therefore continue to refer to this ordered state as the TIA phase.

The interesting feature of the Bragg peaks observed in this applied field data, as compared to the previous zero-field studies, is the much smaller full width at half maximum (FWHM) of the peaks associated with the TIA phase, although they are still significantly broader than the instrumental resolution of WISH. We previously assigned the peak broadening of this phase to the inherent disorder of the TIA state due to its lack of conventional 3D crystallographic order.[36,43] The smaller

**12126** | *J. Mater. Chem. C*, 2020, **8**, 12123–12132

This journal is © The Royal Society of Chemistry 2020

FWHM of this phase in applied field corresponds to a much larger correlation length, likely within the chains of the TIA state.

Raising the field to 0.2 T, increased the intensities of the peaks associated with the TIA phase, and additional intensity was observed on reflections caused by scattering from the nuclear structure, indicating a magnetic phase indexing to a $k_2$-vector = (000) (see Fig. S5 and S6 for quality of selected fits, ESI†). The intensity of the magnetic reflections associated with the $k_2$ phase can be described by a simple ferromagnetic structure, with all moments aligned along the $c$-axis. The alignment of the moments along the $c$-axis, is in agreement with the easy axis and Ising anisotropy of the spins, expected from a $Tb^{3+}$ ion and observed in previous studies.[8,52] At 0.2 T the maximum intensity of the reflections associated with the TIA phase is observed, with a refined magnetic moment of 0.86(7) $\mu_B$. Between 0.2–0.6 T there is phase coexistence of the TIA and the ferromagnetic phase, with the TIA phase dropping in intensity at fields above 0.2 T, and the ferromagnetic phase growing in intensity. Here we have treated the observed magnetic scattering as phase coexistence, however, we cannot rule out that this scattering arises from a single phase of two moments up, and one down. Our preference is for a two phase model due to the presence of these phases existing separately, in zero and higher applied fields. Refinement of a single magnetic phase model produces a worse fit to the data at 0.2 T ($R_{wp\text{-single phase}}$ = 6.79% $vs.$ $R_{wp\text{-dual phase}}$ = 5.90%, 58° bank), due to slight differences in FWHM of peak associated with the two phases, caused by differing correlation lengths.

At 0.8 T only the ferromagnetic phase exists. Scattering from this phase increases in intensity up to 3 T (see Fig. S7 and S8 for this to this data), although it is near saturation (8.63(11) $\mu_B$) at $\sim$2 T, as shown in Fig. 4.

The saturation value at 3 T, 8.86(10) $\mu_B$, is close to the 9 $\mu_B$ value expected for $Tb^{3+}$ from diffraction data, and has excellent agreemen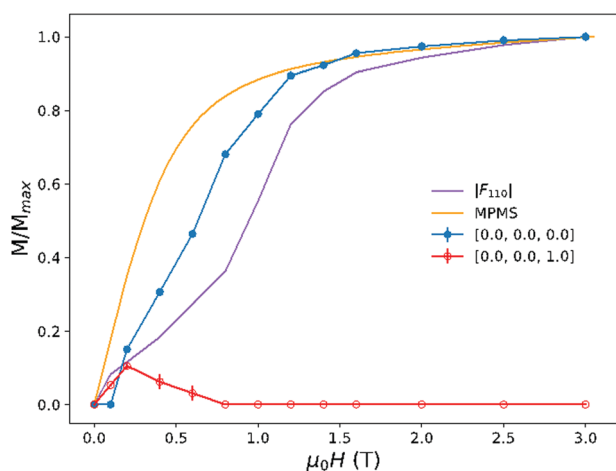t to our magnetic property measurements, validating the accuracy of the neutron diffraction results. We have plotted $M/M_{max}$ to negate the effect of uniaxial magnetic anisotropy on magnetisation data, allowing for comparison to moments refined from neutron data.

The formation of the $k_1$ phase prior to the ferromagnetic phase indicates the small applied fields assists the system to build up long range ordering in the $ab$ plane, until the Zeeman energy is larger than the interchain coupling and a metamagnetic transition occurs to a ferromagnet. That is, the highly entropic short range 1D ferromagnetic correlations that occur in zero field,[36,43] enables the spins within the chains to be readily aligned in magnetic field, transitioning into a ferromagnet (see Fig. 5). This enables the number of microstates and entropy to be greatly and easily reduced.

The alignment of the ferromagnetic chains in the correlated paramagnetic phase, to simple ferromagnetic structure leads to large changes in entropy for small applied magnetic fields, which has been suggested in previous studies.[8,53] In this study we have confirmed and directly observed the evolution from the correlated paramagnetic phase through the TIA phase and ultimately to a ferromagnetic phase under moderate applied fields. This is consistent with the idea that the ferromagnetic chains, in this material, likely play a key role in its optimised magnetocaloric properties under low applied fields and the existence of the TIA plays some role in this.

**Variable temperature measurements in a 0.1 T magnetic field.** In order to confirm whether the TIA phase persists into the temperatures at which the MCE is greatest, we have explored the features associated with this phase under a fixed applied field at variable temperatures.

Variable temperature measurements were performed subsequently to the variable field measurements. Before variable temperature measurements the applied field was removed,
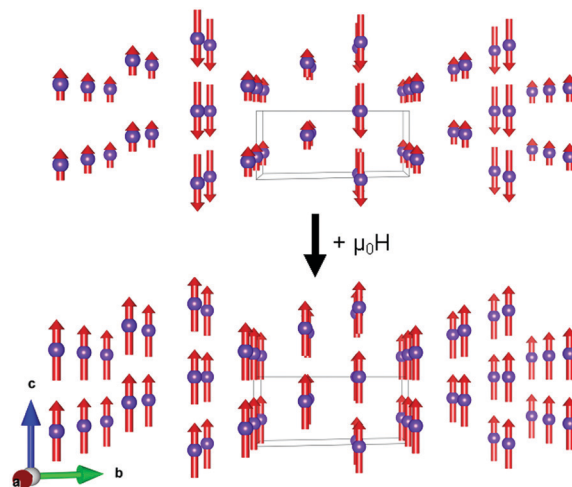


Fig. 4 Evolution of the total ordered magnetic moments associated with $k_1$ (red) and $k_2$ (blue), in $Tb(DCO_2)_3$, with respect to field. Shown in orange is the magnetic moment as determined by the MPMS at 2 K. Shown in purple is the structure factor of the (110) reflection, the most intense peak associated with the ferromagnetic phase.



Fig. 5 Diagram showing the phase transition from a $\frac{1}{2}$ up $\frac{1}{2}$ up down ($k_1$) phase to a ferromagnetic ($k_2$) phase in applied magnetic field. The $Tb^{3+}$ atoms are not to scale and shown in purple, all other atoms have been excluded for clarity and magnetic vectors are shown as red arrows. The unit cell is shown as a black box. Upper figure shows the PDA phase, and the lower shows the ferromagnetic phase along the [100] axis.
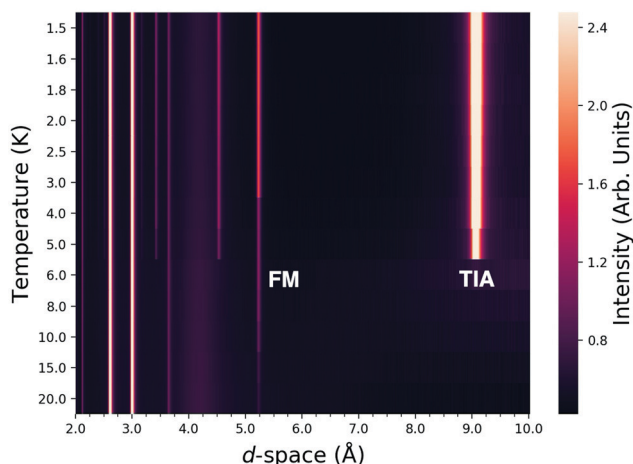
This journal is © The Royal Society of Chemistry 2020

J. Mater. Chem. C, 2020, 8, 12123–12132 | 12127

**Fig. 6** Contour plot of bank 2/9 of WISH for Tb(DCO$_2$)$_3$ with respect to temperature, with a 0.1 T applied field. The weak peaks at ~5.2 Å indicates the ferromagnetic (FM) phase, and the strong peaks at ~9 Å indicates the TIA phase.



**Fig. 7** Evolution of the ordered magnetic moments associated with $\mathbf{k}_1$ (red) and $\mathbf{k}_2$ (blue), in Tb(DCO$_2$)$_3$, with respect to temperature in a 0.1 T applied magnetic field.

heated to 30 K to remove any magnetic correlations, cooled to base, and a 0.1 T field applied and left to equilibrate. Measurements were then taken at variable temperatures, with a 0.1 T applied field, between 1.5 and 40 K. The diffraction patterns are shown in Fig. 6.

All intensity in the reflections is lost upon reaching the critical temperatures of ~8 K, for the TIA phase and between 20 and 40 K for the ferromagnetic phase, respectively (see Fig. 7 for evolution of refined magnetic moments). At 1.5 K in a 0.1 T field we observe phase coexistence of the same $\mathbf{k}_1$ and $\mathbf{k}_2$ phases seen in earlier measurements, with refined moments of 6.57(5) and 3.10(4) $\mu_B$ for the TIA and ferromagnetic phases, respectively, with the greater extent of magnetic order compared to the previous measurements as a function of field. Differences in moment lengths can be attributed to the longer equilibration time at base temperature. Raising the temperature resulted in continuous reductions of the magnetic moments, before a rapid decrease in their intensities above 3 and 4 K for the TIA and ferromagnetic phases. We note that the critical temperature for the TIA phase observed here is higher than that observed in zero applied fields above 1.6 K, confirming it is stabilised by application of an applied magnetic field. Above this temperature diffuse scattering centred around ~9.1 Å/0.5 Å$^{-1}$ is observed (see Fig. S9, ESI†). The diffuse scattering observed is qualitatively similar to that observed in previous studies,[8,36,43] and therefore can likely be attributed to short range 1D Ising chain correlations along the $c$-axis.

### TbODCO$_3$

**Field sweep.** TbODCO$_3$ was cooled in zero applied magnetic field to a base temperature of $T_{base}$ = 1.5 K and left to equilibrate for 1 hour. Measurements as a function of applied magnetic field were then taken between $\mu_0 H$ = 0–3 T in variable steps. The positions of the Bragg reflections associated with the crystal structure do not change significantly under application of magnetic fields indicating there is no significant change in
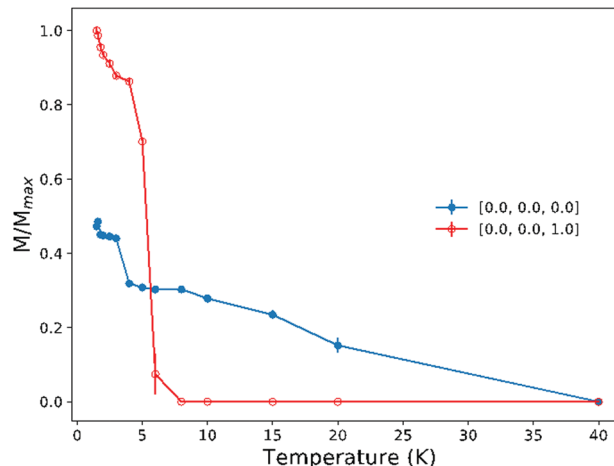
lattice parameters, which was confirmed by refinements. As in zero field measurements of TbODCO$_3$ strong magnetic diffuse scattering is observed in applied fields (see Fig. S10, ESI†).[9,33] The diffuse magnetic scattering observed in these studies (seen between 6–9 Å) are qualitatively similar to the scattering observed in the zero field studies of the LnODCO$_3$ phases. Therefore, this diffuse scattering is likely due to the short range ferromagnetic Ising chain correlations. With the increase in applied magnetic field above 0.2 T additional Bragg peaks evolve as the magnetic diffuse scattering recedes indicating a transition from short to long range order (see Fig. 8). In applied fields larger than 1.4 T the magnetic diffuse scattering effectively disappears, indicating that long range magnetic order is complete. Further analysis of the diffuse background was not possible, in this study, due to the higher background caused by sample environment. The clearest indication of the growing
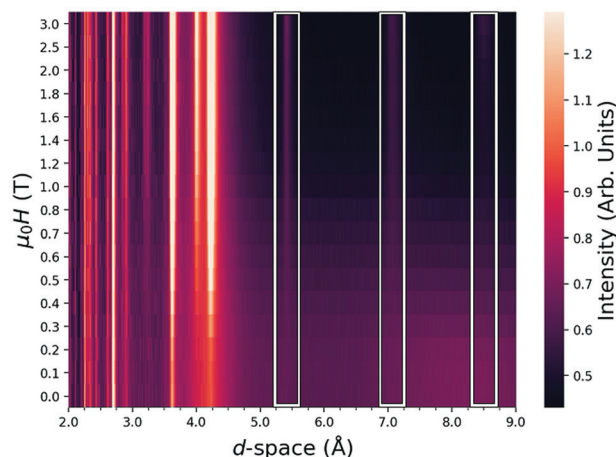


**Fig. 8** Evolution of the ordered magnetic moments associated with the applied field phases of TbODCO$_3$ with respect to applied field. Growing peaks highlighted with boxes, can be seen at 5.3, 7.1 and 8.5 Å with greater applied magnetic fields. There is significant magnetic diffuse scattering at higher $d$-space, from which the Bragg peaks emerge.

12128 | J. Mater. Chem. C, 2020, 8, 12123–12132

This journal is © The Royal Society of Chemistry 2020

long-range ordered magnetic phases is indicated by the Bragg peaks at 5.3, 7.1 and 8.5 Å, which increase with applied magnetic field (see Fig. 8). More detailed studies could be performed in future to establish if there is a phase that can account for the sharp magnetic reflections and the magnetic diffuse that accompanies it under higher applied magnetic fields but quantitative analysis is not possible with the data obtained here due to the partial obscuring of the diffuse scattering by the $d_6$-isopropyl alcohol glass.[54]

Strong magnetic diffuse scattering is observed at higher $d$-spacing, as shown in Fig. 8 and Fig. S8 (ESI†), consistent with previous zero field studies,[9] from which the magnetic Bragg peaks emerge. All magnetic reflections of this material, are associated with the $\Gamma$-point, but cannot be fitted well by a single magnetic phase. Symmetry analysis of the $\mathbf{k} = 0$ propagation vector acting on the $P2_12_12_1$ space group produces four symmetry allowed magnetic structures, three with ferromagnetic components along the $a$, $b$ and $c$-axis and one with no ferromagnetic component. Good fits were obtained with two coexisting $\mathbf{k} = 0$ phases, but combining these into a single phase, which results in lowering the symmetry to $P2_1$ significantly worsens this fit.

In zero applied fields the $\mathbf{k} = 0$ antiferromagnetic structure, with no ferromagnetic component, was observed at low temperatures in HoODCO$_3$.[15] In applied fields this antiferromagnetic phase is not likely to be observed in TbODCO$_3$, as structures would be expected to contain a net ferromagnetic moment that can couple with applied field, consistent with the rapid increase in magnetisation observed in physical property measurements. Inspection of the other three magnetic structures reveals that only those with a ferromagnetic component along the $b$ and $c$ axes, produce a magnetic structure compatible with the reported easy axes of the Tb$^{3+}$ moments.[9] Fitting the data with a model comprised of these two separate magnetic phases leads to excellent fits, as shown in Fig. S11 and S12 (ESI†). Thus the magnetic phase can be described as a coexistence of a ferromagnetic phase and a canted antiferromagnetic phase. The ferromagnetic phase and the canted antiferromagnetic phases both adopt $P2_1'2_1'2_1$ magnetic symmetry and are differentiated by the presence of the $m\Gamma_4$ and $m\Gamma_2$ modes, respectively. The canted antiferromagnetic phase adopts the same unit cell as the nuclear, but the ferromagnetic phase is related to the nuclear unit cell by a $\{(1,0,0),(0,0,-1),(0,1,0)\}$ transformation and a shift of the origin to $(1/4,1/4,-1/4)$. For simplicity all figures are presented in the nuclear unit cell.

The ferromagnetic phase emerges in small magnetic fields ($<0.1$ T) with the canted antiferromagnetic phase coexisting and forming at $<0.2$ T applied fields, both growing with increasing magnetic field above 0.2 T. The ferromagnetic phase has a significant net ferromagnetic component along the $b$-axis (Fig. 9), with non-collinear moments in agreement with the easy axis suggested previously.[9]

This reflects the non-collinear nature of the Ising-like short range ordered phase of TbODCO$_3$. In this long range ordered structure, however, not only are the magnetic cations within the chains ferromagnetically coupled but they also have ferromagnetic inter-chain coupling. This indicates that the applied
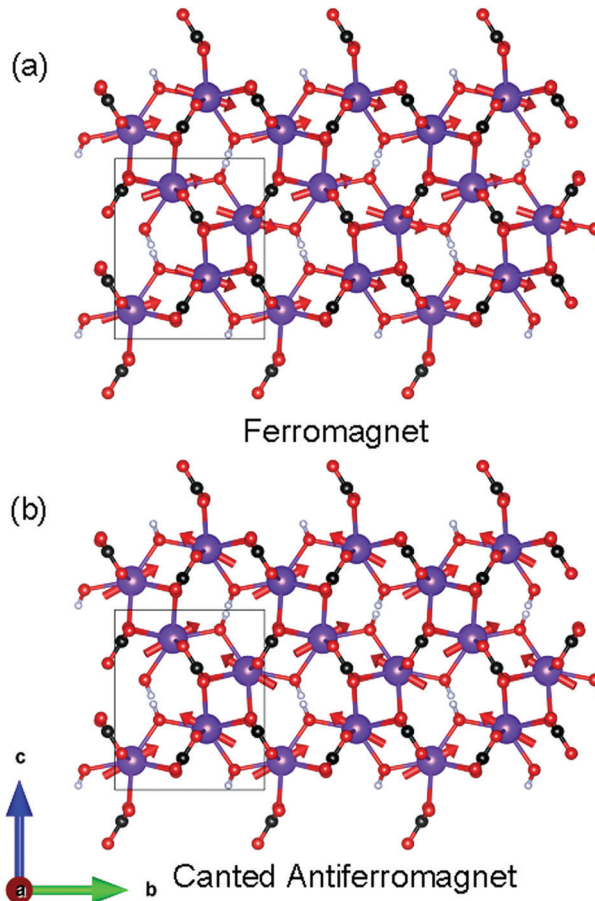


Fig. 9 The two magnetic structures of TbODCO$_3$ in an applied magnetic field at 3 T. Tb$^{3+}$ ions are shown in purple, carbon shown in black, oxygen shown in black and deuterium shown in grey. Unit cell shown in black. Magnetic vectors shown as red arrows. (a) Shows the ferromagnetic structure while (b) shows the canted antiferromagnetic structure, which has a significant ferromagnetic component along the $c$-axis. The magnetic chains are highlight as translucent black lines.

magnetic field has overcome the interchain antiferromagnetic coupling found in the short range ordered phase. The canted antiferromagnetic phase coexisting with a ferromagnetic phase in the presence of a magnetic field initially appeared peculiar since it has antiferromagnetic coupling within its chains, along the $b$-axis, in contrast to the ferromagnetic coupling that is dominant in the short range ordered state in the absence of an applied magnetic field.[15] As seen in Table 1 the refined canted antiferromagnetic phase has non-collinear spins oriented towards the $[\pm0.33, 1, \pm0.66]$ axes with a net ferromagnetic component along the $c$-axis. This contrasts with the ferromagnetic phase where essentially the same easy axis is adopted but the dominant net ferromagnetic moment is along the $b$-axis. These two phases can of course be combined into one phase, however fits were found to be superior in a coexisting two phase model compared to the single phase model ($R_{\text{wp-single phase}} = 4.27\%$ vs. $R_{\text{wp-dual phase}} = 1.85\%$, $58°$ bank), which also produced unphysical moment lengths. Better fits were obtained due to a broader peak FWHM, and therefore

Open Access Article. Published on 14 August 2020. Downloaded on 9/17/2024 1:44:00 PM. This article is licensed under a Creative Commons Attribution 3.0 Unported Licence.

**Table 1** Summary of the LnODCO$_3$ applied field magnetic structures, showing the spin unit vectors of the ferromagnetic (top) and canted antiferromagnetic (bottom) structure at 3 T. The respective $x$, $y$ and $z$ fractional coordinates of Tb1-4 atomic sites are; Tb1 = 0.00554(17), 0.11279(4), 0.16182(3), Tb2 = 0.49446(17), 0.88721(4), 0.66182(3), Tb3 = 0.99446(17), 0.61279(4), 0.33818(3) and Tb4 = 0.50554(17), 0.38721(4), 0.83818(3)

| Atomic site | $u$ | $v$ | $w$ |
|---|---|---|---|
| | Ferromagnet | | |
| Tb1 | 0.152(10) | 0.94(2) | 0.301(11) |
| Tb2 | 0.152(10) | 0.94(2) | −0.301(11) |
| Tb3 | −0.152(10) | 0.94(2) | −0.301(11) |
| Tb4 | −0.152(10) | 0.94(2) | 0.301(11) |
| | Canted antiferromagnet | | |
| Tb1 | 0.223(12) | 0.85(2) | 0.483(11) |
| Tb2 | −0.223(12) | −0.85(2) | 0.483(11) |
| Tb3 | 0.223(12) | −0.85(2) | 0.483(11) |
| Tb4 | −0.223(12) | 0.85(2) | 0.483(11) |



**Fig. 10** Evolution of the ordered magnetic moments associated with the ferromagnetic phases of TbODCO$_3$ with respect to applied field. Shown in blue is the total ordered ferromagnetic moment as determined by Rietveld refinement of the diffraction pattern from neutron diffraction data. Shown in orange is the magnetic moment as determined by the MPMS at 2 K, and purple is the structure factor of the ferromagnetic (002) reflection.

shorter correlation length, in the canted antiferromagnetic phase compared to the ferromagnetic phase.

The difference in the orientation of the net ferromagnetic component in the two observed phases allows the rationalisation of their co-existence by considering the application of an applied field to a polycrystalline sample. The near random particle orientation distribution in powder samples produces suitable powder averaging to allow indexing and characterisation of the nuclear phase in these materials. However with highly anisotropic single ion moments, in the application of a magnetic field sufficient powder averaging is lost. The applied magnetic field acting on each micro-crystallite forces the magnetic moments to align in the most favourable orientation that depends on the orientation of the applied field with respect to that microcrystallite, with consideration of the local Ising easy axis. That is, if the magnetic field vector is applied closer to the $b$-axis of the randomly oriented particle, the ferromagnetic component of the moments will most likely be aligned along the $b$-axis producing the ferromagnetic phase. We hypothesise that the canted antiferromagnetic phase arises when the applied field is closer to the $c$-axis consisting of a ferromagnetic component observed along the $c$-axis, consistent with the observed magnetisation saturation value. We observe no magnetic phase with a ferromagnetic moment along $a$, and hypothesise the strong anisotropy prevents this magnetic phase forming, which would produce magnetic moments orientations that differ from the [±0.33, 1, ±0.66] easy axes reported for the Tb cations, established from previous reverse Monte Carlo studies.[9]

Both structures produce moments with easy axes close to those earlier reported and the long range ordered $\mathbf{k}$ = 0 state seen in HoODCO$_3$,[9] but both have ferromagnetic components along the $b$, and $c$ axes for the ferromagnetic and canted antiferromagnetic structures, respectively. Fig. 10 shows the evolution of the ordered magnetic moments obtained from our refinements. For highly anisotropic single ions such as Tb$^{3+}$, the magnetic moments refined from powder diffraction data must also be considered tentatively, because of constraints used in the refinement and that proper powder averaging is not achieved.
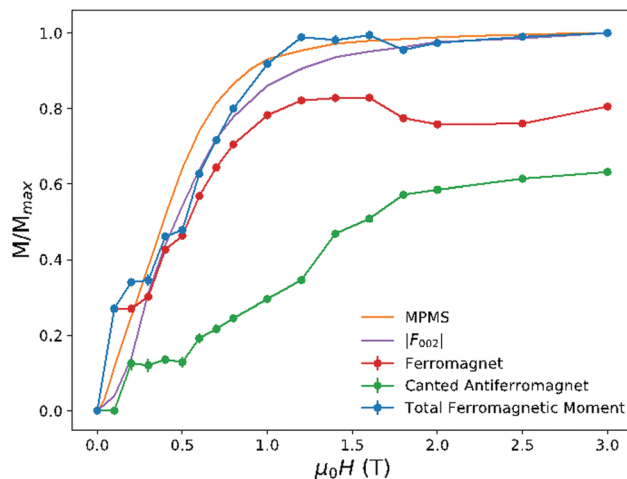
Despite this difficulty, the magnetic structures and moments determined are sensible and in agreement with magnetisation measurements, and therefore confident our model is close to the physical manifestation of these phenomena. We find excellent agreement between our neutron total ferromagnetic moment and magnetisation measurements, saturating at $2/3g_jJ$. We observe the same magnetisation plateau in magnetic form factor, as seen in the magnetisation measurements, at low fields. The co-existence of two $\mathbf{k}$ = 0 magnetic phases lead to the problem of having overlapping reflections, and the inability to refine moment size and phase fraction simultaneously. Contributions from each phase are therefore difficult to de-convolute, so absolute values from each phase are approximations and lead to noisy neutron magnetisation curves. The effect of the applied magnetic field on the evolution of the magnetic phases is also in broad agreement with magnetic susceptibility measurements showing typical magnetisation behaviour and beginning to saturate below 2 T. To completely understand the ground state of this material, for particular directions of applied magnetic fields, neutron diffraction sized single crystals would need to be obtained. This would allow fields to be applied along particular directions of the crystal structure in a more controlled fashion. However, given the challenges in growing large single crystal under hydrothermal conditions this will require considerable synthetic optimisation.

In a 3.0 T magnetic field, at 1.5 K, the ferromagnetic and canted antiferromagnetic phases have magnetic moments of 5.04(6) and 3.95(3) $\mu_B$, respectively. While we cannot determine the moment size and phase fraction of these two phases unambiguously, the ordering of the ferromagnetic phase appears to occur more readily at low applied fields suggesting that only a small magnetic field along specific axis is required to suppress the interchain correlations and align the entire phase ferromagnetically. Furthermore, the ferromagnetic phase
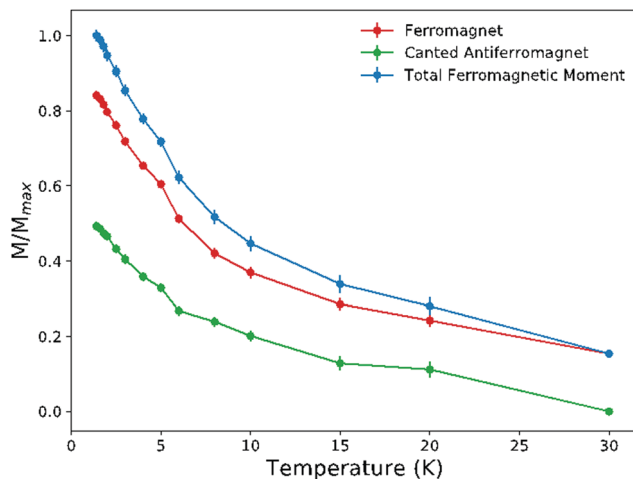
**12130** | *J. Mater. Chem. C*, 2020, **8**, 12123–12132     This journal is © The Royal Society of Chemistry 2020

Fig. 11 Evolution of the ordered magnetic moments associated with the ferromagnetic phases of TbODCO$_3$ with respect to temperature in a 1 T applied field. Blue indicates the ordered magnetic moment as determined by Rietveld refinement of the diffraction pattern from neutron diffraction data.

appears to also have either more complete magnetic order or be the dominant phase compared to the canted antiferromagnetic structure, particularly below 1.8 T. This may indicate that single crystal samples of TbODCO$_3$ magnetised along the $b$-axis may show a single ferromagnetic phase and therefore would have even better magnetocaloric performance in low applied magnetic fields, than the powder analogue. In contrast applying a magnetic field vector along the $c$-axis to a single crystal, of this phase, is likely to only display the canted antiferromagnetic structure described above.

**Variable temperature measurements in a 1 T applied field.** To confirm the persistence of the ordered magnetic phases in TbODCO$_3$ to higher temperatures, and thus their relevance to the MCE, variable temperature measurements have been performed in fixed magnetic fields. TbODCO$_3$ was warmed to 20 K, and the field was set to $\mu_0H = 0$ T, to remove any magnetic order. The sample was then cooled to $T_{base} = 1.5$ K and a 1.0 T magnetic field was applied. A 1.0 T field was seen to be an appropriate field to apply due to the efficient magnetocaloric performance of TbODCO$_3$ in a 1.0 T field changes over a wide temperature range. In the presence of a 1.0 T magnetic field, measurements were taken between 1.5 and 30 K in variable steps. At $T_{base}$ the magnetic peaks are clearly present, indicating the presence of both ferromagnetic and antiferromagnetic $P2_1'2_1'2_1$ phases. The length of total ferromagnetic moment is 5.49(12) $\mu_B$, consisting of ferromagnetic moments of 4.62(6) $\mu_B$, and antiferromagnetic moments of 2.71(6) $\mu_B$. Raising the temperature with the applied magnetic field resulted in a continuous reduction of the magnetic moments of both phases, as can be seen in Fig. 11.

The continued presence of this ferromagnetic phase in a magnetic field to high temperatures, through the temperature range where TbOHCO$_3$ has been found to have high magnetocaloric performance,[33] indicates it readily forms under an applied magnetic field, which is beneficial to its magnetocaloric properties.

## Conclusions

We have observed the mechanism for the magnetocaloric effect in two highly efficient low temperature magnetocaloric materials, with applications in liquid helium refrigeration replacement, through neutron diffraction. Our results show that the application of a magnetic field drives the transition from high entropy correlated paramagnetic phases, containing ferromagnetic Ising chains, to low entropy ordered phases. Specifically we suggest that the significant ferromagnetic correlations are of greatest importance in these materials enabling ordered magnetic states to emerge at low fields, once the frustrated antiferromagnetic interactions are suppressed. The short-range ordered states contain a greater number of microstates, compared with the ordered states, such that when a magnetic field is applied a large change in microstates and entropy is observed ($\Delta S = R \ln \Omega$), resulting in large magnetocaloric effect. At sufficiently low temperatures the limit for entropy changes for random Ising spins approaches $R \ln 2$,[26,54,55] but the correlated disordered nature of these materials maximises accessible entropy changes for low applied fields.[8,33] Crucially, we have shown that such ordered states persist to temperatures above which the peak magnetocaloric properties are observed, such they are likely to play a key role in this performance. This has great implications in the design of new magnetocaloric materials optimised for low temperature refrigeration, and liquid helium replacement. The insights gained from this study highlight the power of neutron diffraction to provide significant insight into magnetic materials exhibiting unusual field induced transitions.

Here we have shown clearly that ferromagnetic Ising chains play a key role in the adiabatic refrigeration cycle of two promising materials, Tb(DCO$_2$)$_3$ and TbODCO$_3$. These correlations allow Tb(DCO$_2$)$_3$ and TbODCO$_3$ to outperform similar Ising magnetocaloric materials in low fields at these temperatures.[26,46]

## Conflicts of interest

There are no conflicts to declare.

## Acknowledgements

## References

1 R. L. Comstock, *J. Mater. Sci.: Mater. Electron.*, 2002, **13**, 509–523.
2 F. S. Guo, B. M. Day, Y. C. Chen, M. L. Tong, A. Mansikkamäki and R. A. Layfield, *Science*, 2018, **362**, 1400–1403.

This journal is © The Royal Society of Chemistry 2020

*J. Mater. Chem. C*, 2020, **8**, 12123–12132 | **12131**

3 Z. Luo, A. Hrabec, T. P. Dao, G. Sala, S. Finizio, J. Feng, S. Mayr, J. Raabe, P. Gambardella and L. J. Heyderman, *Nature*, 2020, **579**, 214–218.

4 Y. D. Xiao, R. Paudel, J. Liu, C. Ma, Z. S. Zhang and S. K. Zhou, *Int. J. Mol. Med.*, 2016, **38**, 1319–1326.

5 R. D. Johnson, P. Barone, A. Bombardi, R. J. Bean, S. Picozzi, P. G. Radaelli, Y. S. Oh, S. W. Cheong and L. C. Chapon, *Phys. Rev. Lett.*, 2013, **110**, 217206.

6 C. Vecchini, A. Bombardi, L. C. Chapon, N. Lee, P. G. Radaelli and S. W. Cheong, *J. Phys.: Conf. Ser.*, 2014, **519**, 012004.

7 M. M. Vopson, *Solid State Commun.*, 2012, **152**, 2067–2070.

8 P. J. Saines, J. A. M. Paddison, P. M. M. Thygesen and M. G. Tucker, *Mater. Horiz.*, 2015, **2**, 528–535.

9 R. C. Dixey, G. B. G. Stenning, P. Manuel, F. Orlandi and P. J. Saines, *J. Mater. Chem. C*, 2019, **7**, 13111–13119.

10 J. L. Liu, Y. C. Chen and M. L. Tong, *Chem. Rec.*, 2016, **16**, 825–834.

11 L. Mañosa, A. Planes and M. Acet, *J. Mater. Chem. A*, 2013, **1**, 4925–4936.

12 J. L. Manson, Q. Z. Huang, J. W. Lynn, H. J. Koo, M. H. Whangbo, R. Bateman, T. Otsuka, N. Wada, D. N. Argyriou and J. S. Miller, *J. Am. Chem. Soc.*, 2001, **123**, 162–172.

13 M. Kurmoo, *Chem. Soc. Rev.*, 2009, **38**, 1353–1379.

14 P. J. Saines, M. Steinmann, J. C. Tan, H. H. M. Yeung, W. Li, P. T. Barton and A. K. Cheetham, *Inorg. Chem.*, 2012, **51**, 11198–11209.

15 Z. Hulvey, B. C. Melot and A. K. Cheetham, *Inorg. Chem.*, 2010, **49**, 4594–4598.

16 A. E. Thorarinsdottir and T. D. Harris, *Chem. Rev.*, 2009, **38**, 1353–1379.

17 N. J. Robinson, F. H. L. Essler, I. Cabrera and R. Coldea, *Phys. Rev. B: Condens. Matter Mater. Phys.*, 2014, **90**, 174406.

18 I. Cabrera, J. D. Thompson, R. Coldea, D. Prabhakaran, R. I. Bewley, T. Guidi, J. A. Rodriguez-Rivera and C. Stock, *Phys. Rev. B: Condens. Matter Mater. Phys.*, 2014, **90**, 014418.

19 R. Coldea, D. A. Tennant, E. M. Wheeler, E. Wawrzynska, D. Prabhakaran, M. Telling, K. Habicht, P. Smeibidl and K. Kiefer, *Science*, 2010, **327**, 177–180.

20 T. J. S. Munsie, M. N. Wilson, A. Millington, C. M. Thompson, R. Flacau, C. Ding, S. Guo, Z. Gong, A. A. Aczel, H. B. Cao, T. J. Williams, H. A. Dabkowska, F. Ning, J. E. Greedan and G. M. Luke, *Phys. Rev. B: Condens. Matter Mater. Phys.*, 2017, **96**, 144417.

21 M. Nandi and P. Mandal, *J. Appl. Phys.*, 2016, **119**, 133904.

22 J. D. Bocarsly, E. E. Levin, S. A. Humphrey, T. Faske, W. Donner, S. D. Wilson and R. Seshadri, *Chem. Mater.*, 2019, **31**, 4873–4881.

23 A. M. Tishin and Y. I. Spichkin, *Mater. Today*, 2003, **6**, 51–52.

24 J. Lyubina, *J. Phys. D: Appl. Phys.*, 2017, **50**, 053002.

25 A. Smith, *Eur. Phys. J. H*, 2013, **38**, 507–517.

26 P. Mukherjee and S. E. Dutton, *Adv. Funct. Mater.*, 2017, **27**, 1701950.

27 P. Mukherjee, A. C. Sackville Hamilton, H. F. J. J. Glass and S. E. Dutton, *J. Phys.: Condens. Matter*, 2017, **29**, 405808.

28 P. Mukherjee, H. F. J. Glass, E. Suard and S. E. Dutton, *Phys. Rev. B: Condens. Matter Mater. Phys.*, 2017, **96**, 140412.

29 J. A. M. Paddison, H. Jacobsen, O. A. Petrenko, M. T. Fernández-Díaz, P. P. Deen and A. L. Goodwin, *Science*, 2015, **350**, 179–181.

30 J. A. Barclay and W. A. Steyert, *Cryogenics*, 1982, **22**, 73–80.

31 R. Moessner and A. P. Ramirez, *Phys. Today*, 2006, **59**, 24–29.

32 Y.-C. Chen, L. Qin, Z.-S. Meng, D.-F. Yang, C. Wu, Z. Fu, Y.-Z. Zheng, J.-L. Liu, R. Tarasenko, M. Orendáč, J. Prokleška, V. Sechovský and M.-L. Tong, *J. Mater. Chem. A*, 2014, **2**, 9851–9858.

33 R. J. C. Dixey and P. J. Saines, *Inorg. Chem.*, 2018, **57**, 12543–12551.

34 G. Lorusso, J. W. Sharples, E. Palacios, O. Roubeau, E. K. Brechin, R. Sessoli, A. Rossin, F. Tuna, E. J. L. McInnes, D. Collison and M. Evangelisti, *Adv. Mater.*, 2013, **25**, 4653–4656.

35 P. J. Saines and N. C. Bristowe, *Dalton Trans.*, 2018, **47**, 13257–13280.

36 R. J. C. Dixey, F. Orlandi, P. Manuel, P. Mukherjee, S. E. Dutton and P. J. Saines, *Philos. Trans. R. Soc., A*, 2019, **377**, 20190007.

37 L. C. Chapon, P. Manuel, P. G. Radaelli, C. Benson, L. Perrott, S. Ansell, N. J. Rhodes, D. Raspino, D. Duxbury, E. Spill and J. Norris, *Neutron News*, 2011, **22**, 22–25.

38 H. M. Rietveld, *J. Appl. Crystallogr.*, 1969, **2**, 65–71.

39 J. Rodríguez-Carvajal, *Phys. B*, 1993, **192**, 55–69.

40 A. Le Bail, *Powder Diffr.*, 2005, **20**, 316–326.

41 J. Rodriguez-Carvajal, M. T. Fernandez-Diaz and J. L. Martinez, *J. Phys.: Condens. Matter*, 1991, **3**, 3215–3234.

42 J. M. Perez-Mato, S. V. Gallego, E. S. Tasci, L. Elcoro, G. de la Flor and M. I. Aroyo, *Annu. Rev. Mater. Res.*, 2015, **45**, 217–248.

43 D. R. Harcombe, P. G. Welch, P. Manuel, P. J. Saines and A. L. Goodwin, *Phys. Rev. B: Condens. Matter Mater. Phys.*, 2016, **94**, 174429.

44 D. Brunt, G. Balakrishnan, D. A. Mayoh, M. R. Lees, D. Gorbunov, N. Qureshi and O. A. Petrenko, *Sci. Rep.*, 2018, **8**, 232.

45 K. Siemensmeyer, E. Wulf, H. J. Mikeska, K. Flachbart, S. Gabáni, S. Mat'Aš, P. Priputen, A. Efdokimova and N. Shitsevalova, *Phys. Rev. Lett.*, 2008, **101**, 177201.

46 P. Mukherjee, Y. Wu, G. I. Lampronti and S. E. Dutton, *Mater. Res. Bull.*, 2018, **98**, 173–179.

47 P. Mukherjee, E. Suard and S. E. Dutton, *J. Phys.: Condens. Matter*, 2017, **29**, 405807.

48 Z. He, J. I. Yamaura, Y. Ueda and W. Cheng, *J. Am. Chem. Soc.*, 2009, **131**, 7554–7555.

49 H. Kageyama, K. Yoshimura, K. Kosuge, H. Mitamura and T. Goto, *J. Phys. Soc. Jpn.*, 1997, **66**, 1607–1610.

50 P. Lampen-Kelley, E. M. Clements, B. Casas, M. H. Phan, H. Srikanth, J. Marcin, I. Skorvanek, H. T. Yi and S. W. Cheong, *J. Magn. Magn. Mater.*, 2020, **493**, 165690.

51 M. Nandi, N. Khan, D. Bhoi, A. Midya and P. Mandal, *J. Phys. Chem. C*, 2014, **118**, 1668–1673.

52 R. Skomski and D. J. Sellmyer, *J. Rare Earths*, 2009, **27**, 675–679.

53 R. Li, P. Manuel, F. Orlandi and C. Greaves, *J. Mater. Chem. A*, 2018, **6**, 21149–21155.

54 J. A. M. Paddison, H. S. Ong, J. O. Hamp, P. Mukherjee, X. Bai, M. G. Tucker, N. P. Butch, C. Castelnovo, M. Mourigal and S. E. Dutton, *Nat. Commun.*, 2016, **7**, 13842.

55 W. P. Wolf, *Braz. J. Phys.*, 2000, **30**, 794–810.

**12132** | *J. Mater. Chem. C*, 2020, **8**, 12123–12132

This journal is © The Royal Society of Chemistry 2020